Measurement-induced phase transitions in the toric code

Amir-Reza Negari, Subhayan Sahu, and Timothy H. Hsieh

Perimeter Institute for Theoretical Physics, Waterloo, Ontario N2L 2Y5, Canada
and Department of Physics and Astronomy, University of Waterloo, Waterloo, Ontario N2L 3G1, Canada

We show how distinct phases of matter can be generated by performing random single-qubit measurements on a subsystem of toric code. Using a parton construction, such measurements map to random Gaussian tensor networks, and in particular, random Pauli measurements map to a classical loop model in which watermelon correlators precisely determine measurement-induced entanglement. Measuring all but a 1d boundary of qubits realizes hybrid circuits involving unitary gates and projective measurements in 1+1 dimensions. We find that varying the probabilities of different Pauli measurements can drive transitions in the unmeasured boundary between phases with different orders and entanglement scaling, corresponding to short- and long-loop phases in the classical model. Furthermore, by utilizing single-site boundary unitaries conditioned on the bulk measurement outcomes, we generate mixed-state ordered phases and transitions that can be experimentally diagnosed via linear observables. This demonstrates how parton constructions provide a natural framework for measurement-based quantum computing setups to produce and manipulate phases of matter.

I. INTRODUCTION

Investigating the quantum phases of matter that can be dynamically generated in a quantum processor using measurement, classical feedback, and local unitaries has been a fruitful area of research. There has been significant interest in using such hybrid circuits to manipulate entanglement patterns, starting with the observation of a measurement-induced entanglement transition between volume law to area law as the frequency of measurements is varied [1–9] (for a review, see [10,11]). Even without any unitary gates, random measurements of multisite operators can lead to not only various entanglement patterns but also distinct long-range orders, such as symmetry-protected topological order, spin-glass order, and intrinsic topological order [12–15]. These orders can undergo phase transitions by adjusting the probabilities of competing measurements.

A different context in which measurements take center stage is measurement-based quantum computation (MBQC) [16]. The MBQC approach involves starting with an entangled "resource state", such as the 2d cluster state, and sequentially performing single site measurements on the majority of the qubits, where the measurement basis can depend on the outcomes of previous measurements. This results in the remaining unmeasured qubits being directed towards a specific entangled state that encodes the outcome of a deterministic quantum computation. For example, measurements on a 2d resource state effectively realize a computation on the 1d boundary of the system, and the other dimension corresponds to the "time" direction of the computation.

In this paper, we ask the question: Starting with an entangled resource state, can MBQC-type protocols lead to robust quantum phases of matter and transitions between them? We explore this question for the toric code ground state, which is an exactly solvable model of $\mathbb{Z}_2$ topological order in two

dimensions [17]. We find that by tuning the probabilities of measuring single-site Pauli X, Y, or Z in the toric code bulk, we can realize distinct phases in an unmeasured boundary. These measurement-induced phases are characterized by the presence or absence of spin-glass order parameters and their entanglement scaling (area law vs logarithmic scaling). As is the case for MBQC, the bulk measurements in the toric code effectively realize dynamics for a one-dimensional boundary, and in this case the effective dynamics are that of a hybrid circuit involving both unitaries and measurements. Thanks to the underlying entanglement of the toric code state, only single-qubit measurements are required to effectively realize nontrivial hybrid circuits involving two-qubit operations.

Liu *et al.* [18] performed a related study on the 2d cluster state, an MBQC resource state, which enables universal quantum computation, and discovered an entanglement transition from area to volume law in boundary qubits induced by measuring the bulk qubits. In contrast, in our setup with toric code, we find transitions in both entanglement (albeit without volume law) and other order parameters. A recent study [19] also considered an MBQC setup on the 2d cluster state and found evidence of distinct area law entanglement phases on the 1d boundary. One advantage of our setup is that we can understand such transitions analytically by relating the entanglement properties of the qubits to certain correlation functions of a corresponding 2d classical loop model with crossings. Such a model has short- and long-loop phases, which exactly correspond to the area law and the logarithmic scaling of entanglement in the 1d boundary. The summary of these results is presented in Fig. 1. We also note that Ref. [20] established a very different mapping between toric code error correction in the presence of both incoherent and coherent errors and $(1 + 1)$d free-fermion circuits.

As is the case with hybrid circuits without feedback (measurement outcomes are not used to inform future operations),
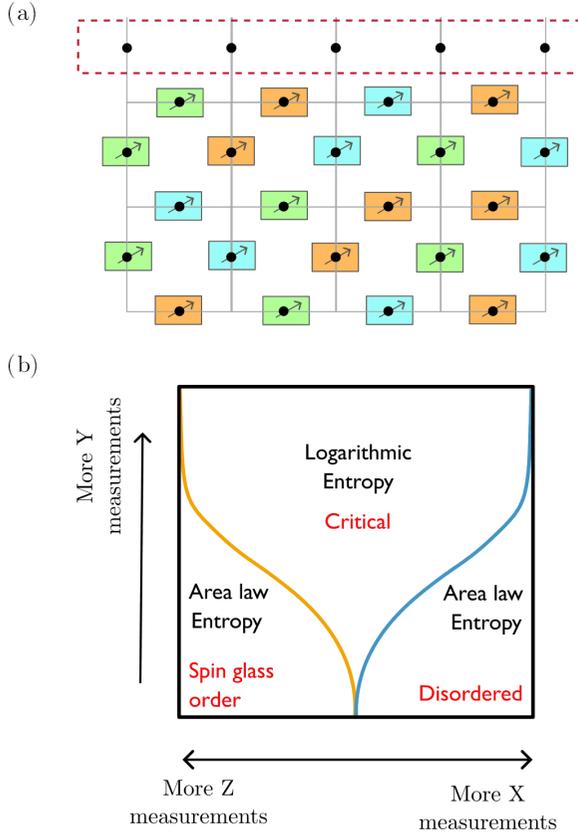
FIG. 1. (a) The bulk of a toric code ground state is measured in random Pauli bases (denoted by different colors), which induces correlations between the unmeasured 1d boundary qubits (in dashed box). (b) Depending on the relative frequencies of different Pauli measurements, the 1d boundary can have different entanglement scaling (area law vs logarithmic scaling) and also different orders (spin-glass vs paramagnetic). Such phases and transitions are analyzed by mapping to a 2d classical loop model.

the transition between quantum phases is only apparent in quantities nonlinear in the ensemble of quantum trajectories. In our examples, these nonlinear quantities can be spin-glass order parameters or entanglement measures. However, the spin-glass order can be converted into ferromagnetic order (a linear observable) via feedback: We show that one layer of single-qubit unitaries, conditioned on the bulk measurement outcomes, can be applied to the boundary state to ensure that the resulting density matrix averaged over trajectories has long-range order that is observable. This constitutes a nontrivial quantum channel on a 2d array producing a long-range entangled mixed state in 1d; as in [21], it relies on measurement and unitary feedback, although the resulting mixed state is likely difficult to generate using only operations on the 1d system.

This setup can be readily generalized from Pauli X, Y, Z measurement to arbitrary single-site projective measurements. We find that such measurements in $2 + 0$d map in general to Gaussian fermionic hybrid circuits in $1 + 1$d. This mapping allows us to import the results about entanglement phases generated by such circuits (e.g., [22–24]) onto the measurement-induced entanglement on the boundary state

of the toric code. Even in the general on-site measurement setup, the phases with area law and logarithmic scaling of entanglement persist, albeit with distinct phase boundaries and transitions.

The structure of the paper is as follows: In Sec. II, we introduce the measurement setup for toric code. We then map the stabilizer configurations after measurements to the completely packed loop model with crossing (CPLC) and summarize relevant results in Sec. III. In Sec. IV, we relate specific order parameters in the loop model to entanglement induced by measurements between different regions. In Sec. V, we explain how the mapping leads to distinct entanglement patterns in unmeasured boundary qubits and we demonstrate how the setup can be mapped to a 1+1d hybrid circuit. In Sec. VI, we show how the presence or absence of a certain spin glass order distinguishes the two phases. Furthermore, we describe a simple adaptive protocol that modifies the boundary state and enables identification of the two phases based on linear-order parameters of the state. In Sec. VII we analyze general single-qubit measurements (beyond Pauli) on the toric code and map the resulting states to Gaussian tensor networks and Gaussian hybrid circuits. This section also contains a tensor network representation of the toric code ground state via parton construction, which may be of independent interest. Finally, in Sec. VIII we conclude with a discussion of our results, including relations to the underlying sign structure and MBQC universality of the resource state.

II. SETUP

A. Toric code/plaquette model

The toric code is a lattice model of spin-1/2 degrees of freedom on the edges of a square lattice [17], which consists of commuting terms in its Hamiltonian called stabilizer operators. The toric code has two types of stabilizer operators: star (s) and plaquette (p) operators,

$$H_T = -\sum_s \prod_{j \in s} X_j - \sum_p \prod_{j \in p} Z_j. \tag{1}$$

A closely related model is Wen's 2d plaquette model [25], where the spin-1/2 degrees of freedom are located at the vertices of a square lattice, and the Hamiltonian consists of only one type of four-body stabilizer for every star s and plaquette p, on the 45°-rotated lattice [see Fig. 2(a)],

$$H_W = -\sum_{a \in p, s} X_{a+\hat{y}} Z_{a+\hat{x}} X_{a-\hat{y}} Z_{a-\hat{x}}. \tag{2}$$

These two models can be transformed into each other using a single layer of local Hadamard gates arranged on one (say, B) of the two sublattices (A and B) of the square lattice in the plaquette model. Sublattice A represents spins on vertical edges, while sublattice B represents spins on horizontal edges of toric code in Fig. 2(b). These gates interchange $X \leftrightarrow Z$ on the B sublattice, which interchange the plaquette model and toric code, as depicted in Fig. 2(a). On a torus defined by identifying the boundaries along x, y directions as marked in Fig. 2(b), the toric code has four degenerate ground states, labeled by ± 1 eigenvalues of the logical operators O'_1, O'_2. These logical operators can be obtained by applying the
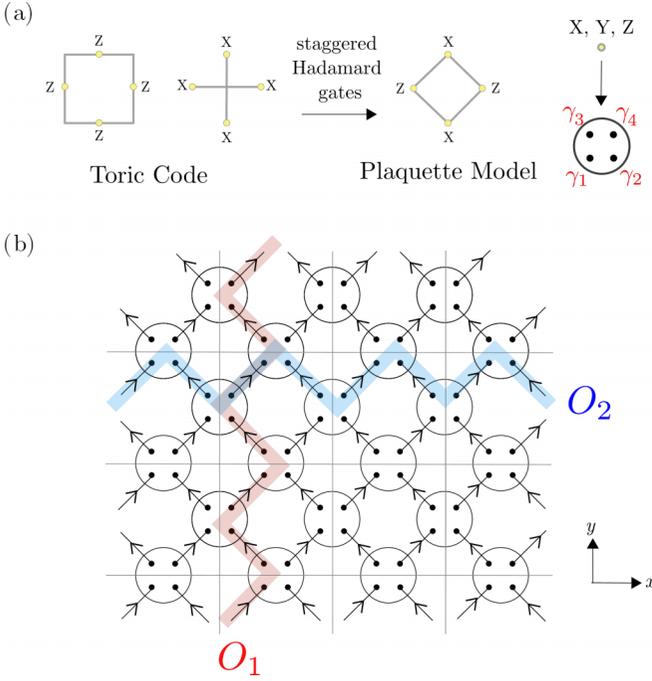
FIG. 2. (a) Toric code stabilizers can be converted to Wen plaquette stabilizers via staggered Hadamard gates. The Wen plaquette admits a parton construction in which each qubit is split into four Majorana fermions subject to a constraint (represented by circle in right subfigure). (b) A ground state of the plaquette model can be constructed by projecting a free-fermion state consisting of Majorana dimers into the physical qubit Hilbert space.

previously mentioned Hadamard gates to Wen's logical operators O_1 and O_2, which consist of strings of Pauli-Z and Pauli-X operators as depicted in Fig. 2(b).

Any eigenstate $|G\rangle$ of the toric code admits an exact free-fermion parton construction [25,26] defined as follows. The Hilbert space of each qubit on site i can be enlarged into that of four Majorana fermions $\gamma_{i,s} = \{\gamma_{i,1}, \gamma_{i,2}, \gamma_{i,3}, \gamma_{i,4}\}$ along the edges connected to i, followed by a projection onto the original qubit Hilbert space. Consider the free-fermion state $|\psi\rangle_{\text{free}}$ such that $i\gamma_{i,s}\gamma_{j,s'} = 1$ when $(i,s), (j,s')$ are on the same edge. To return the qubit Hilbert space, we must project the Majorana state to the $+1$ sector of the operator $D_j = \gamma_{j,1}\gamma_{j,2}\gamma_{j,3}\gamma_{j,4}$,

$$|G\rangle = \prod_j \left(\frac{1+D_j}{2}\right)|\psi\rangle_{\text{free}}. \tag{3}$$

Note that the initial free-fermion state of the two Majorana modes on neighboring vertices can be oriented in two different ways, depending on whether we take the $+1$ eigenstate of $\pm i\gamma_{i,s}\gamma_{j,s'}$. Different orientations [which are marked by $s \to s'$ to indicate $+i\gamma_s\gamma_{s'}$ in Fig. 2(b)] determine the particular eigenstate up to a global phase. In particular, the ground space of the toric code on a torus is four dimensional; one representative ground state is described in our convention by the orientation shown in Fig. 2(b), where the same orientation is taken along all 45° lattice lines. Different logical sectors (choices of $O_1, O_2 = \pm1$) of the plaquette model ground space can be represented by flipping all the orientations of the links ij

along the nontrivial loops. We will focus our attention on the ground state defined by the orientation shown in Fig. 2(b), which corresponds to $O_1, O_2 = +1$.

B. Measurement setup

First we consider the case of measuring a subset of qubits M in the toric code in either Z, Y, or X bases, with respective probabilities $(1-q)(1-p)$, p, and $q(1-p)$, which we call the (p,q) measurement protocol. Our objective is to analyze the entanglement structure and order in the remaining (unmeasured) qubits M^c after the measurements on M are performed. The target quantities of interest are averaged over all realizations of both measurement configurations and their outcomes. In a later section, we will generalize to the case of measuring along any direction in the Bloch sphere.

Due to the equivalence between the toric code and plaquette models via a Hadamard transformation on one sublattice, the (p,q) scheme for toric code is equivalent to the (p,q) scheme on A sublattice and $(p, 1-q)$ scheme on B sublattice for the plaquette model.

In the plaquette model, Pauli operators on site j correspond to Majorana fermion bilinear operators

$$
\begin{aligned}
X_j &= i\gamma_{j,1}\gamma_{j,2} = i\gamma_{j,4}\gamma_{j,3}, \\
Y_j &= i\gamma_{j,2}\gamma_{j,3} = i\gamma_{j,4}\gamma_{j,1}, \\
Z_j &= i\gamma_{j,1}\gamma_{j,3} = i\gamma_{j,2}\gamma_{j,4},
\end{aligned} \tag{4}
$$

where the right equalities follow from the physical Hilbert space condition ($D_j = 1$).

C. Stabilizers and measurement

We first provide a brief overview of the Majorana stabilizer formalism specialized to our setting. The set of stabilizer generators $\mathcal{G}$ is a set of products of Majorana fermions, which are independent and mutually commute with each other. This set generates the stabilizer group $\mathcal{S}$. In a Hilbert space of dimension 2^N, a set $\mathcal{G}$ with exactly N generators uniquely defines the common eigenvector $|\psi\rangle$ of any operator generated by $\mathcal{G}$, such that $s|\psi\rangle = |\psi\rangle \; \forall s \in \mathcal{S}$.

If we measure the state $|\psi\rangle$ with an operator P, which is a product of Majorana fermions, the resulting state is still a Majorana stabilizer state and can be updated efficiently [27,28]. There are two cases to consider. If P commutes with all the stabilizer generators $g \in \mathcal{G}$, the measurement will not have any effect on the state, and the measurement outcome can be inferred from the sign of the operator in $\mathcal{S}$, i.e., whether $\pm P \in \mathcal{S}$. If P anticommutes with some of the stabilizer generators, the measurement outcome ± 1 with equal probability. We also have to modify the set of generators $\mathcal{G}$—first we select one of the anti-commuting generators, denoted as g_0, and multiply g_0 with the remaining anticommuting generators. Next, we replace g_0 in $\mathcal{G}$ by either $\pm P$ depending on the measurement outcome, so that the new stabilizer set becomes $\{\pm P\} \cup \{g_0 g_i | \; \forall i \neq 0, g_i$ anticommutes with $P\} \cup \{g_i | \; g_i$ commutes with $P\}$.

The stabilizer formalism offers a way to confirm that the ground state $|G\rangle$ is the projected free-fermion state $|\psi\rangle_{\text{free}}$, stabilized by two-point Majorana fermion operators: $i\gamma_{j,s}\gamma_{i,s'}$. The action of projection operators on the stabilizers
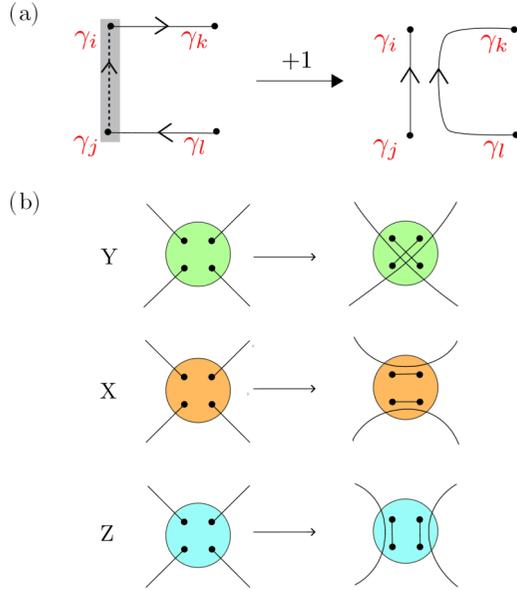
FIG. 3. (a) The update process for measuring the Majorana bilinear $i\gamma_j\gamma_i$ for a free-fermion state, which is a tensor product of Majorana dimers. The $+1$ refers to the measurement outcome, which sets the arrow direction in the final state. If the measurement outcome is -1 the final arrows need to be reversed (detailed analysis in part Sec. II C). (b) Updated pairings from measuring X, Y, and Z Pauli operators on each site of the plaquette model. The updated pairings need to be tiled to form the global dimer state. We have neglected the sign tracking of the dimer pairs, which depends on the measurement outcomes.

exclusively modifies adjacent Majorana pairs by multiplying them together to form string operators. By applying all the projections, these string operators eventually become closed loops, forming Majorana loop operators, which act as stabilizers for the ground state in Wen's model. Our goal is to measure Pauli operators corresponding to different two-point Majorana operators on every site. Since these are physical qubit operators, they commute with the projection operator, and hence we can first consider their effect on the free-fermion state before applying the projection operator at the end.

We graphically track the free-fermion state updates by connecting Majorana fermions with a line when they form a stabilizer operator together. When $i\gamma_j\gamma_i$ is measured, there are two possible outcomes: (a) If there is already a connection between γ_i and γ_j in the initial state, no further updates are required, and (b) if these two Majorana fermions are connected to other Majoranas (e.g., γ_i is connected to γ_k and γ_l is connected to γ_j), the update will connect γ_j to γ_i, and the other Majoranas will be connected accordingly (e.g., γ_l to γ_k), as shown in Fig. 3(a).

The signs of stabilizers and measurement outcomes can be tracked and updated by using arrows on Majorana pairings, as illustrated in Fig. 3(a). However, the signs will not be important when computing entanglement quantities or spin-glass order parameters, in the case of X, Y, Z, i.e., stabilizer, measurements. In the next sections, we will suppress the arrow notation for signs and return to the task of sign-tracking when

discussing the linear order parameter in Sec. VI and on-site measurements in general directions in Sec. VII.

III. COMPLETELY PACKED LOOP MODEL

Measuring Pauli operators on each site generate different patterns of pairings [Fig. 3(b)], and measuring all qubits tiles these patterns and results in different configurations of loops on a square lattice. On the two different sublattices of the square lattice, the factors q and $1 - q$ must be swapped, to reflect the staggered measurement scheme of the plaquette model.

Consider a configuration of measurements or tilings, with the N_x, N_y, N_z number of X, Y, Z measurements performed. Such a configuration has probability $W_\mathcal{C} = p^{N_y}[(1 - p)q]^{N_x}[(1 - p)(1 - q)]^{N_z}$, which leads to the partition function $Z = \sum_\mathcal{C} W_\mathcal{C}$. The model and partition function are known as the completely packed loop model with crossings (CPLC), whose properties have been extensively studied in Ref. [29]. We will now review its important properties relevant to the questions addressed in this paper.

In Ref. [29] the authors found that the phase diagram consists of a short-loop phase and a long-loop "Goldstone" phase, which are separated by a phase transition (see Fig. 4). This model can be described by the replica limit $n \to 1$ of a $\mathbb{Z}_2$ lattice gauge theory coupled to $O(n)$ matter field. Its continuum description is a sigma model, which is massive in the short-loop regime and massless in the Goldstone phase [29].

We focus on two order parameters, which distinguish the phases. First, we consider the *watermelon correlation functions* $G_k(i, j)$, which denote the probability that k distinct strands connect points i and j, where k is even for the CPLC model. For instance, G_4 is the probability that two nodes are connected by four distinct strands. Using renormalization group (RG) techniques on the sigma model Ref. [29] found that in the Goldstone phase

$$G_k(i, j) \sim \frac{C_0}{\ln(d_{ij}/r_0)^{k(k-1)}}, \quad (5)$$

where d_{ij} is the distance between i, j and C_0, r_0 are nonuniversal constants. In the short-loop phases on the other hand, the watermelon correlators decay as $G_k(i, j) \sim e^{-d_{ij}/\xi}$, with correlation length ξ.

Next, we consider the *spanning number* defined for a CPLC model on a cylinder, with two circular open boundaries. The spanning number counts the number of strands that connect the upper and lower boundaries; Ref. [29] found that in the Goldstone phase, the average spanning number scales with system size L as

$$n_s \approx \frac{1}{2\pi}\left(\ln\frac{L}{L_0} + \ln\ln\frac{L}{L_0}\right), \quad (6)$$

whereas it asymptotes to 0 in the short-loop phase.

To explore the entanglement properties of the toric code after measurements and their connection to the phase transitions in the loop model, we need to leave some qubits unmeasured as measuring all qubits results in a trivial pure product state. Three scenarios are considered (see schematic description in Fig. 4):
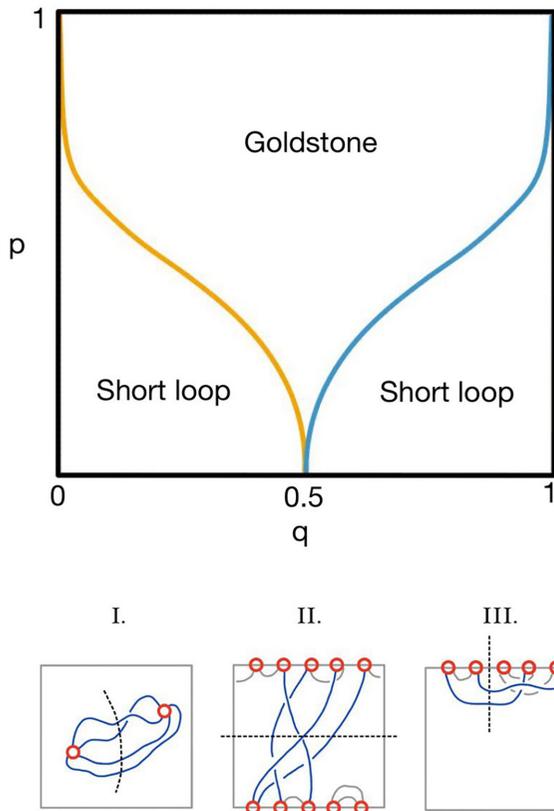
FIG. 4. The schematic phase diagram of the completely packed loop model with crossings (CPLC) [29]. The diagram distinguishes between different phases based on three order parameters, highlighted in the panel below. These order parameters correspond to loop configurations that connect points marked by red dots. The first order parameter (I) quantifies the probability of four distinct strands connecting two red points on a torus, referred to as the "watermelon correlation function." The second order parameter (II) measures the expected number of strands connecting the top and bottom boundaries on a cylinder, known as the "spanning number." The third order parameter (III) measures the expected number of strands connecting two partitions of the top boundary on a cylinder with a fixed boundary condition at the bottom. All three quantities govern measurement-induced entanglement in the toric code state.

(I) *Measuring all but two qubits in the bulk.* In Sec. IV A we show that the entanglement induced between the two measured qubits is directly related to the watermelon correlation function.

(II) *Measuring all but two boundaries.* In Sec. IV B, we observe that the induced entanglement between the two boundaries of the cylinder is directly related to "spanning number" order parameter discussed in this section. Accordingly, in the short-loop phase, the entanglement is asymptotically zero, while in the Goldstone phase, it exhibits logarithmic scaling with the system size.

(III) *Measuring all but a single boundary.* We show in Sec. V that in this case the entanglement between contiguous bipartitions of the unmeasured boundary exhibit a phase transition between area law and logarithmic law, reflecting the underlying loop model configurations.
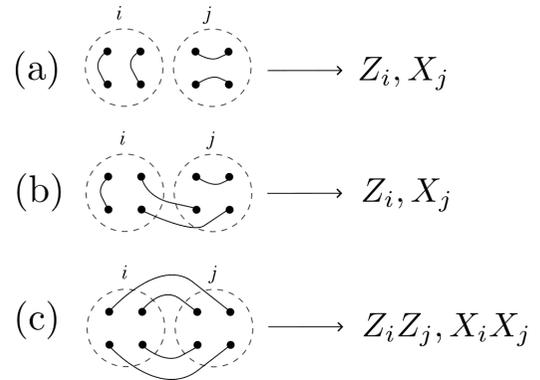

FIG. 5. Three possible pairings of unmeasured qubits i, j after all other qubits are measured. (Left) Stabilizer strands prior to physical qubit Hilbert space projections. (Right) Stabilizers after projections, in canonical form. Note, in writing the stabilizers as Pauli strings, we have assumed that the sites i, j are in the same sublattice. Configurations a and b [in (a) and (b) respectively] are exclusively supported on i or j and do not contribute entanglement, while configuration c [in (c)] contributes one bit of entanglement.

IV. MEASUREMENT-INDUCED ENTANGLEMENT BETWEEN TWO DISTANT REGIONS

In this section, we establish a connection between the average measurement-induced entanglement (MIE) of two distant unmeasured regions and various order parameters within the CPLC model. The MIE has been related to the underlying sign structure of the measured wavefunction in Ref. [30], and we will comment more on this in the concluding discussion.

A. MIE between two unmeasured qubits

We first demonstrate that the measurement-induced entanglement (MIE) between two unmeasured qubits at sites i and j is equivalent to the watermelon correlation $G_4(i, j)$.

Recall that measuring a qubit specifies a given pairing for the four Majoranas associated with the qubit. After all pairings at all sites except for i, j are specified, we must implement the projection operators D_k on every site, as in Eq. (3). Crucially, any *closed loop Majorana stabilizer commutes with the projection operator* and is thus shared by both the free fermion and the projected state in Eq. (3). However, if two qubits are left unmeasured, then some Majorana stabilizers may be open strands ending at the unmeasured sites. In this case the projection operator has a significant effect on the final stabilizers and hence the entanglement between the unmeasured qubits.

To compute the measurement-induced entanglement, we analyze the three ways (Fig. 5) in which Majorana stabilizer strands terminate at the two vertices i, j. (Any closed loop not coincident with i and j will not contribute any entanglement.) Denote a stabilizer strand connecting Majoranas $\gamma_{i,s}$ and $\gamma_{i',s'}$ as $(i_s i'_{s'})$. We suppress the sign information of the stabilizer in this notation. The three classes of configurations are

(a) Each strand ends on Majoranas on the same vertex, i.e., we have two $(i_s i_{s'})$ and two $(j_s, j_{s'})$ pairings.

(b) Two strands end on the same vertex and two strands end on different vertices, i.e., there are one $(i_s i_{s'})$, two $(i_s, j_{s'})$, and one $(j_s, j_{s'})$ pairings.

(c) All four strands terminate in different vertices, i.e., there are four $(i_s, j_{s'})$ pairings.

Once we impose the local projection operators $D_i = (i_1 i_2 i_3 i_4)$, $D_j = (j_1 j_2 j_3 j_4)$, the stabilizer generators need to be updated. Furthermore, to compute the entanglement between the two unmeasured qubits, we choose a canonical gauge for the stabilizers [4,31] for a given bipartition, stabilizer generators restricted to either subsystems are independent. In this canonical form, the entanglement across a bipartition is proportional to the number of stabilizers shared between both parties.

We show examples of the stabilizer update into its canonical form in Fig. 5. In the right column in Fig. 5, we show the stabilizer generators obtained from these patterns of strands, set in their canonical form such that the stabilizer generators restricted to either i or j are independent. As can be seen, the number of such independent *connecting* stabilizers are 0,0, and 2 respectively, in the three types of Majorana pairings a, b, and c. Thus, only configuration c contributes one bit of entanglement, and the average measurement-induced entanglement (MIE) generated between any two unmeasured qubits on i and j is exactly given by the probability of four distinct loops connecting i and j in the CPLC model, i.e., the watermelon correlation function defined in the previous section,

$$\langle S_{\mathrm{MIE}}(i, j)\rangle = \left(G_4^{\mathrm{CPLC}}(i, j)\right) \ln 2. \tag{7}$$

Hence it follows from the results in Ref. [29] as quoted in Eq. (5) that the averaged MIE is long-ranged in the Goldstone phase and short ranged in the short-loop phase.

B. MIE between two unmeasured boundaries

Now we consider the toric code on a cylinder and explore the effects of bulk measurements on the boundary chains of qubits; in particular, we focus on the scenario where both circular boundaries of the toric code are left unmeasured. For the purposes of this section, the exact boundary conditions do not matter, so we defer a discussion on the exact boundary conditions and the exact mapping of this scenario to the loop model to the next section. Here we just quote the final result that under the Majorana loop mapping, the average entanglement between these two boundaries can be directly mapped to the "spanning number" in the loop model, as illustrated in Fig. 4(II).

This can already be motivated from discussions in the earlier subsection, where we showed that the entanglement between the two remote regions of the toric code corresponds to open strands connecting the regions in the CPLC model. However, we must also transform the stabilizers to their canonical forms in order to directly count their entanglement contribution. In Sec. I B within the Supplemental Material (SM) [32] we show that in this geometry, if there are $n \geqslant 2$ such strands connecting the top and bottom boundaries in the loop model, we get $n - 2$ independent Majorana stabilizer generators in their canonical form connecting the top and bottom boundaries. The average n is just the spanning number of the loop model, so we get the following correspondence:

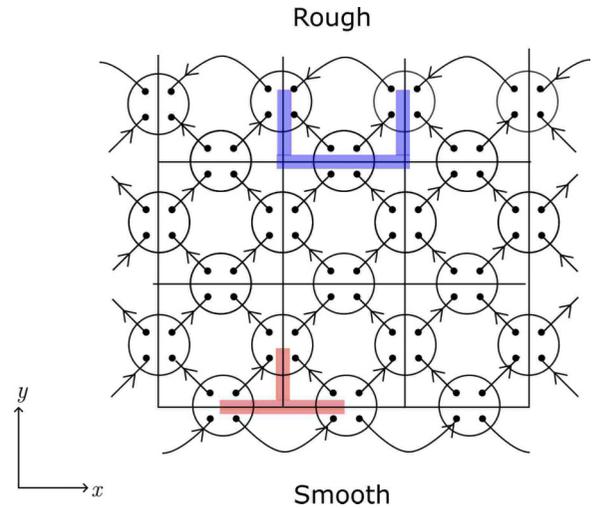$$\langle S_{\mathrm{MIE}}\rangle = \frac{(n_s - 2)\ln 2}{2}. \tag{8}$$

FIG. 6. Boundary conditions of the parton ground state of toric code on cylinder. The rough and smooth boundary conditions on two open edges of the cylinder are shown, along with the respective truncated stabilizers on the boundaries. The x direction is taken to have periodic boundary condition.

This correspondence holds true only for $n_s \geqslant 2$, otherwise, we have $S_{\mathrm{MIE}} = 0$. As noted in Eq. (6), the average spanning number n_s scales logarithmically with L in the Goldstone phase and asymptotes to zero in the short-loop phase.

V. MEASUREMENT-INDUCED PHASE TRANSITION IN THE BOUNDARY

In this section, we investigate the occurrence of measurement-induced phase transitions in a 1d chain of qubits on the boundary of a toric code state, where the remaining qubits are measured in random local Pauli bases (as depicted in Fig. 1). Many of the findings in this section can be generalized to different topologies (such as torus, cylinder, or plane) and partitioning schemes of the unmeasured 1d chain.

We begin by examining a toric code implemented on a cylinder with two open circular boundaries. The boundary stabilizers are truncated, resulting in two types of boundary conditions: "rough" or "smooth". The rough condition arises when the plaquette stabilizers are truncated, while the smooth condition occurs when the star stabilizers are truncated. In Fig. 6, the truncated toric code represented in the parton picture exhibits a simple form, where no distinction between rough and smooth is evident. Consequently, it is unnecessary to specify the type of boundary condition for the entanglement analysis. Moreover, various boundary conditions for the surface code can be created by measuring the toric code state on a torus, followed by applying a single layer of local unitary updates based on the measurement outcomes. For instance, to achieve a surface code with smooth boundary conditions, one should perform Pauli-X measurements along a horizontal line on sub-lattice A. Conversely, a surface code with rough boundary conditions can be formed by conducting Pauli-Z measurements along a horizontal line on sublattice B. Applying both of these measurement patterns results in the surface

	Sublattice	
	B	A
↗	Y	Y
↗	Z	X
↗	X	Z

⊠	Swap	
⌣	Parity Meas.	
)(	Identity	

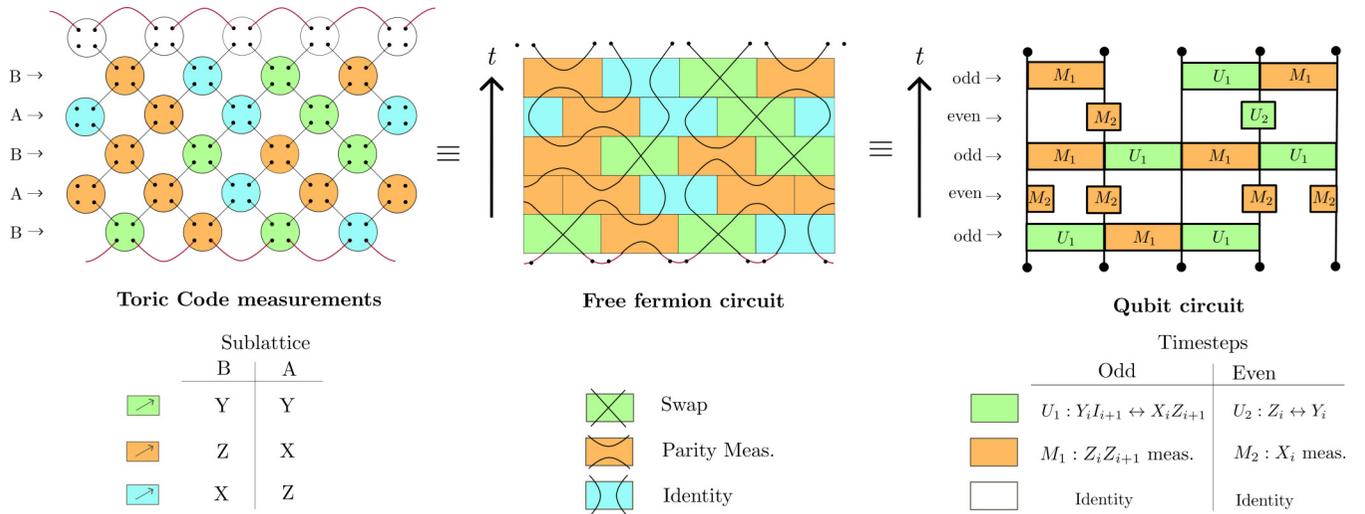|	Timesteps	
	Odd	Even
🟩	$U_1 : Y_i I_{i+1} \leftrightarrow X_i Z_{i+1}$	$U_2 : Z_i \leftrightarrow Y_i$
🟧	$M_1 : Z_i Z_{i+1}$ meas.	$M_2 : X_i$ meas.
⬜	Identity	Identity

FIG. 7. Pauli-$X/Y/Z$ measurements on the bulk, with the boundary chain of qubits left unmeasured (left panel), correspond to a hybrid circuit with measurement and unitary gates. The measurement model is equivalent to a staggered measurement protocol on the Wen plaquette model. The plaquette model generates Majorana pairing patterns in that can be interpreted as world lines of Majorana fermions undergoing a free-fermion hybrid circuit (middle panel). By Jordan-Wigner transformation, the same circuit can be identified with an Ising symmetric measurement and unitary circuit on qubits (right panel).

code illustrated in Fig. 6, featuring both rough and smooth boundary conditions. For concreteness, we will hereafter assume the pair of rough and smooth boundary conditions for the surface code.

In this section, we show that the boundary state after bulk measurements is precisely the state generated by a hybrid circuit in $1 + 1$d composed of measurements and unitaries. While this identification is general, for the particular case of the toric code, the corresponding hybrid circuit is a $1 + 1$d Ising symmetric circuit [12,33]. Our mapping is motivated by MBQC, whereby a circuit can be effectively realized by single-site measurements on a resource state. However, the toric code is not a universal resource state [34]; thus, single-site measurement on the toric code cannot represent all circuits.

A. Measured toric code as a $1 + 1$d hybrid circuit

Starting from the parton representation of the toric code, measuring each qubit modifies the pairings of four neighboring Majoranas, as described in Sec. II. These pairings can be interpreted as world lines of two Majoranas undergoing circuit operations. In particular, the corresponding circuit consists of the following gates acting on two neighboring Majorana fermions: swap gate, identity gate, and fermion parity measurement, as illustrated in the bottom of Fig. 7. Thus, starting from an $N \times N$ toric code state on a cylinder, the bulk measurements realize a depth N free fermion circuit on $2N$ Majorana fermions (Fig. 7 middle panel). Note that for a fixed configuration of measurement bases, different measurement outcomes correspond to hybrid circuits in $1 + 1$d differing only in the signs of the Majorana stabilizers. However, as noted earlier, the observables we are interested in—entanglement and spin-glass order—are not sensitive to these signs and only depend on the worldline connectivity.

Thus, for these observables, the hybrid circuits for a given measurement bases configuration are equivalent, regardless of the outcomes.

After all the projections onto the physical qubit Hilbert space are imposed, the Majorana hybrid circuit maps via Jordan-Wigner transformation to a depth N hybrid circuit of local unitaries and local measurements on a one-dimensional system of N qubits. This mapping is shown explicitly in Fig. 7. We note that this mapping is somewhat subtle, as the parton construction and Jordan-Wigner transformation are two different mappings from one qubit to respectively four and two Majorana fermions. Briefly, the reason why the claimed mapping works is because at the top boundary, the top two of the four Majoranas per parton decomposition are always paired in a nearest-neighbor dimer state (Fig. 7, left), so the physical qubit state is solely determined by the bottom two Majoranas per site via the standard Jordan-Wigner mapping (see Sec. II within the SM [32] for details).

The Majorana fermion parity measurements realize the measurements of either the neighboring $Z_k Z_{k+1}$ or on-site X_k measurement in the qubit circuit, depending on which sublattice the measurements are performed,

$$M_1 = i\tilde{\gamma}_{k,2}\tilde{\gamma}_{k+1,1} = Z_k Z_{k+1},$$
$$M_2 = i\tilde{\gamma}_{k,1}\tilde{\gamma}_{k,2} = X_k. \tag{9}$$

Similarly, the Majorana swap gate implements either a two-qubit unitary U_1 or on-site unitary U_2,

$$U_1 : Y_k I_{k+1} \leftrightarrow X_k Z_{k+1},$$
$$U_2 : Z_k \leftrightarrow Y_k. \tag{10}$$

These circuit operations preserve an Ising $\mathbb{Z}_2$ symmetry $\prod_i X_i$. The origin of this Ising symmetry of the hybrid circuit is the fact that the $\prod_i X_i$ string operator, supported on the rough boundary, takes definite value for the initial surface code

TABLE I. Circuit mapping of the (p, q) measurement model on the toric code (TC). For completeness, the corresponding staggered measurement protocol for the Wen plaquette (WP) model is mentioned in the parentheses.

Sublattice (timesteps)	Measurement TC (WP)	Probability	Qubit Circuit
B (odd)	Y (Y)	p	U_1
	X (Z)	$(1-p)q$	Identity
	Z (X)	$(1-p)(1-q)$	M_1
A (even)	Y (Y)	p	U_2
	X (X)	$(1-p)q$	M_2
	Z (Z)	$(1-p)(1-q)$	Identity

state, and any bulk measurement away from the boundary commutes with this boundary operator.

The qubit circuit corresponding to the (p, q) measurement protocol on the toric code (TC) state can be explicitly defined as follows (see also Table I):

(1) In odd times, perform one of the following operations on each pair of neighboring qubits: two-qubit unitary U_1 (TC measurement along Y) with probability p, identity operation with probability $(1-p)q$ (TC measurement along X), and M_1 measurement with probability $(1-p)(1-q)$ (TC measurement along Z).

(2) In even times, perform one of the following operations on each qubit: on-site unitary U_2 with probability p(TC measurement along Y), on-site measurement M_2 with probability $(1-p)q$ (TC measurement along X), identity operation and with probability $(1-p)(1-q)$ (TC measurement along Z).

B. Bipartite entanglement in the unmeasured boundary

By identifying the bulk Majorana pairings with the classical loop model as in Sec. III, we can establish a direct mapping between the entanglement across a bipartition of the boundary state and a specific quantity depicted schematically in Fig. 4(III) within the loop model. This quantity, which counts the number of strands connecting two parts of the boundary chain, diagnoses the long-range correlations in the Goldstone phase of the loop model.

We also show in Sec. I A within the SM [32] that for the one boundary setup, there is a one-to-one correspondence between the Majorana strands and the canonical stabilizer generators after implementing projections. Specifically, a configuration with n open strands connecting the two parts of the boundary corresponds to a quantum state with n canonical stabilizer generators connecting the two parts, thereby contributing $\frac{n \ln 2}{2}$ units of entanglement. The bipartite entanglement between two parts of the boundary thus acts as an order parameter for the phase transition in the loop configurations of the CPLC model.

In the Goldstone phase of CPLC, Ref. [33] found that the entanglement between a contiguous subregion A of the qubit chain has a logarithmic scaling with a correction. Therefore, the entanglement of a contiguous subregion A of the unmeasured boundary chain of the toric code also satisfies the same

entanglement scaling in the Goldstone phase,

$$\langle S_A \rangle \approx \frac{\ln(2)}{2} \left(\# \ln |A| + \frac{1}{4\pi} (\ln |A|)^2 \right), \quad (11)$$

while it obeys an area law in the short-loop phase.

VI. LONG-RANGE ORDER IN THE BOUNDARY STATE

A. Spin-glass order parameter

As we showed in the previous section, the bulk measurements performed on the toric code can be mapped to the Ising-symmetric hybrid circuits studied by Sang *et al.* [12,33]. Given only ZZ measurements, the steady state is a "random GHZ" state characterized by a random spin configuration superposed with the flipped configuration. This is also known as a spin-glass state, and the spin-glass order is captured by the Edwards-Anderson order parameter,

$$O = \frac{1}{L} \sum_{i,j}^{L} \langle \psi | Z_i Z_j | \psi \rangle^2. \quad (12)$$

For spin-glass order, $O \sim L$, whereas for paramagnetic order, $O \sim O(1)$.

Reference [12] studied the phase diagram of hybrid circuits involving ZZ and X measurements and random Ising-symmetric Clifford unitaries, and a stable spin-glass phase was found. The toric code measurements map to a subset of symmetric Clifford unitaries—namely, the free-fermion operations defined above—and for this restricted class we provide a fermionic perspective on the spin-glass order parameter and the extent of the spin-glass phase.

The central object in the spin-glass order parameter is $Z_i Z_j$, which for a stabilizer state can take three values (± 1 or 0). It maps via Jordan-Wigner transformation to

$$Z_i Z_j = i \gamma_{i,2} \left(\prod_{k=i+1}^{k=j-1} i \gamma_{k,1} \gamma_{k,2} \right) \gamma_{j,1}. \quad (13)$$

This string of Majoranas is nonzero if and only if all Majoranas within the interval (i, j) are paired amongst themselves. (If any Majorana within the interval is paired with one outside, that dimer will anticommute with the above string and render its expectation value zero.)

In the short-loop phase, configurations are composed of loops with a characteristic size ξ, which is independent of L. Hence, the probability that all Majoranas within an interval (i, j) are paired up is independent of $|i - j|$ for $|i - j| \gg \xi$. For $q < 1/2$, this probability is a nonzero $O(1)$ number independent of $|i - j|$, and thus the spin-glass order parameter is extensive in the $q < 1/2$ short-loop phase.

B. Linear-order parameter from adaptive circuits

Due to the equal probabilities of $Z_i Z_j$ having opposite signs ± 1, its average value is zero, making it necessary to use nonlinear order parameters such as the Edwards-Anderson order parameter defined in Eq. (12). However, in experimental setups, measuring nonlinear order parameters is generally challenging and requires postselection of the measurement outcomes. In practice it is more feasible to access expectation

values of operators like $\mathrm{Tr}(\rho O)$ which are linear in the density matrix ρ, the ensemble of all measurement trajectories.

Here we detail an efficient protocol for converting the (nonlinear) spin-glass order into a linear-order parameter. Our protocol employs an adaptive strategy that applies a layer of local unitaries on the boundary conditioned on the bulk measurement outcomes. The main objective of this adaptive unitary layer is to transform all the $\pm$ values of $Z_i Z_j$ stabilizer generators into positive values, thus eliminating the issue of sign cancellation and converting the spin-glass order into long-range ferromagnetic order, which is linear in the state and can be accessed experimentally. The protocol consists of two main parts: (1) identify $Z_i Z_j$ stabilizers and determine their signs, and (2) obtain single-site unitaries that can correct the negative signs to positive signs.

Note that one approach for identifying and correcting the sign of $Z_i Z_j$ operators in the stabilizer group is to simulate the entire evolution classically using the stabilizer formalism, with the knowledge of all the $O(L^2)$ bulk measurement outcomes. However, we propose a simpler algorithm that only requires access to the directions and outcomes of measurements within a correlation length $O(\xi)$ from the boundary, i.e., $O(L\xi)$ measurements.

The algorithm is as follows:

A. $Z_i Z_j$ **generator graph construction**: We construct a graph whose vertices are the boundary qubit sites i and which has an edge ij if $\pm Z_i Z_j$ is in the stabilizer group. By knowing the positions of X, Y, Z measurements, we can obtain the corresponding configuration of Majorana strands. If for any $i < j$, $\gamma_{j,2}$ is paired up with $\gamma_{j,1}$, we draw an edge ij in the graph. As per Eq. (13), this pairing implies a $Z_i Z_j$ stabilizer if and only if all the Majorana fermions in the interval (i, j) are paired up internally. This can be checked for all the Majorana fermions in (i, j) from the loop configuration. If indeed there are strands that exit the interval (i, j), then we erase the edge ij in the graph as this does not correspond to a $Z_i Z_j$ stabilizer. For the special case $p = 0$ without loop crossings, this second step is not necessary, as all the Majorana strands must be nested in this case. Note that the graph is a tree as the Majorana strands are all independent generators.

We then obtain the sign of the $Z_i Z_j$ stabilizers by tracking the sign of the arrows along the strand $\gamma_{j,2}\gamma_{j,1}$ and all the intermediate strands $\gamma_{k,1}\gamma_{k',2}$ for $k, k' \in (i, j)$. This requires us to keep track of only $O(L\xi)$ measurement outcomes, where ξ is the correlation length corresponding to the loop size in the underlying CPLC model. If $Z_i Z_j = -1$, we color the edge ij.

B. Correcting the sign: From the previous step, we have a colored graph. Flipping a spin k (acting with the unitary X_k) changes the signs of all adjacent edges to the node k. We can correct any negative sign on an edge by flipping all nodes on one side of the edge [see Fig. 8(c)]. Repeating this process for each edge allows us to flip the sign of every edge individually. To correct all the edges with a minimal number of operations, a search algorithm within the tree can be performed, which has a polynomial complexity with respect to the system size.

Given access to the measurement protocol and outcomes, this algorithm (with complexity polynomial in system size) can be executed by a classical computer to determine the necessary adaptive unitary protocol, resulting in all trajectories having non-negative $Z_i Z_j$ correlations. The resulting ensemble
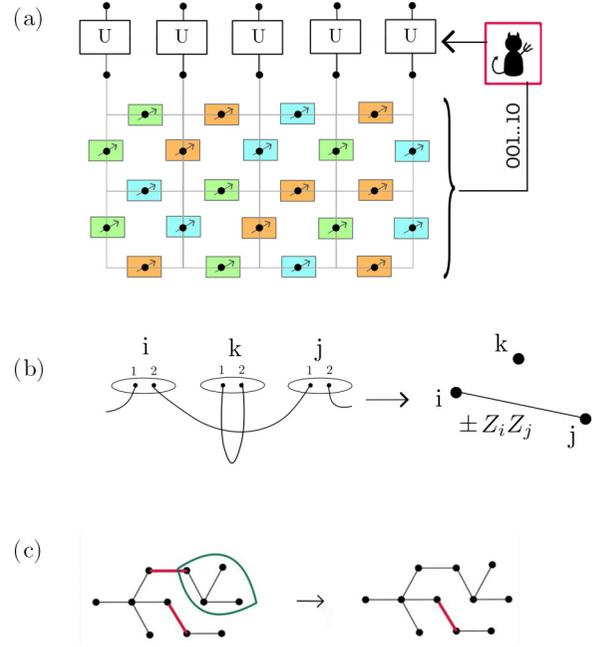

FIG. 8. (a) To convert any (nonlinear) spin-glass long-range order of the boundary state into (linear) ferromagnetic long-range order, a layer of on-site unitaries conditioned on bulk measurement outcomes can be applied to the boundary. (b) The classical processing for the adaptive protocol involves using the distribution of Majorana strands to construct a graph in which an edge between nodes (qubits) i, j represents existence of a $Z_i Z_j$ stabilizer. The edges are colored depending on whether the sign of the stabilizer is ± 1, which can be computed from the measurement outcomes along the strands. (c) The negative signs in the tree graph can be flipped by applying X_k on all nodes on one side of the negative edge (e.g., those encircled).

of trajectories ρ has long-range ferromagnetic order $\langle Z_i Z_j \rangle_\rho$ in the original spin-glass phase.

VII. GENERAL ON-SITE MEASUREMENTS

We now consider the effect of measurements along an arbitrary direction $n_x X + n_y Y + n_z Z$ on the toric code. These map to statistical models that go beyond the scope of the previously discussed CPLC model (Sec. III). In the following, we will demonstrate the representation of the measured toric code using Gaussian tensor networks (GTN) and the realization of Gaussian hybrid circuits within the virtual space. Furthermore, we will establish a connection with well-studied Gaussian hybrid circuits to showcase the robustness of the boundary MIE phase diagram obtained from the CPLC model in the general measurement case.

A. Tensor network representation of parton construction

The parton representation of the toric code state can be reinterpreted as a two-dimensional tensor network composed of local tensors $|T\rangle$. These tensors consist of a single physical leg representing a qubit and four virtual legs representing the parton Majorana fermions. To construct a tensor network, contractions between spins or contractions between Majorana
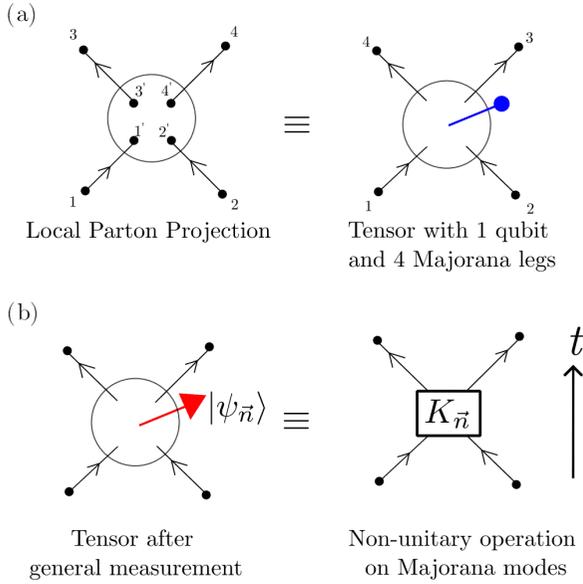
(a)

Local Parton Projection

Tensor with 1 qubit
and 4 Majorana legs

(b)

Tensor after
general measurement

Non-unitary operation
on Majorana modes

FIG. 9. (a) The parton representation of the toric code state can be interpreted as a local tensor with one "physical" qubit leg and four "virtual" Majorana legs, along with an orientation for contraction of the virtual indices. In this case, the orientation corresponding to a toric code ground state is specified. (b) Measuring the parton state, or equivalently, contracting the physical index with a state vector in a general direction, leads to a Gaussian state on the four "virtual" Majorana degrees of freedom. This Gaussian state can be mapped to a Gaussian operation on two Majorana fermions, and can be directly identified with a nonunitary operator.

fermions are allowed. A contraction between spins involves projecting the two legs onto a maximally entangled state, and a contraction between Majorana fermions sharing an edge involves projecting the two Majorana fermions onto the eigenstate of the $i\gamma_i\gamma_j$ operator with eigenvalue $+1$. The latter assumes an orientation for each virtual bond which must be specified.

We now describe the tensor network representation of the projected parton states of the toric code. First, we introduce

the projection tensor that maps four Majorana fermions to one spin,

$$P = \frac{|G_1\rangle\,|\uparrow\rangle + |G_2\rangle\,|\downarrow\rangle}{\sqrt{2}}. \quad (14)$$

Here $|G_1\rangle$ and $|G_2\rangle$ are two fermionic stabilizer states of the four Majoranas, where $|G_1\rangle$ is stabilized by $i\gamma_1\gamma_3$, $i\gamma_2\gamma_4$ and $|G_2\rangle = i\gamma_1\gamma_2\,|G_1\rangle$. The orientation for bonds between tensors is specified in Fig. 9(a), and corresponds to the orientation of Majorana pairs described in Sec. II.

B. Measured toric code as a Gaussian tensor network

Measuring a qubit in the $\vec{n}$ axis and obtaining outcome ±1 corresponds to contracting the physical leg of a tensor with the qubit state $|\psi_{\pm\vec{n}}\rangle$, the eigenstate of operator $\vec{n}\cdot\vec{\sigma} = n_x X + n_y Y + n_z Z$ with eigenvalue ±1. After contraction, the resulting projection tensor takes the form of a Gaussian fermionic tensor on the remaining Majorana legs,

$$|F_{\vec{n}}\rangle = \frac{|G_1\rangle\,\langle\psi_{\vec{n}}|\,|\uparrow\rangle + |G_2\rangle\,\langle\psi_{\vec{n}}|\,|\downarrow\rangle}{\sqrt{2}}$$

$$= \frac{e^{i\phi}\cos\frac{\theta}{2}\,|G_1\rangle + \sin\frac{\theta}{2}\,|G_2\rangle}{\sqrt{2}}. \quad (15)$$

Here, θ and ϕ represent the spherical coordinates of the unit vector $\vec{n} = (n_x, n_y, n_z) = (\sin\theta\cos\phi, \sin\theta\sin\phi, \cos\theta)$. The fermionic operators F^1 and F^2 which stabilize $|F_{\vec{n}}\rangle$ (meaning that $F^{1,2}\,|F_{\vec{n}}\rangle = |F_{\vec{n}}\rangle$) are

$$F^1 = i\gamma_1\gamma_3\cos\theta + i\gamma_1\gamma_2\sin\theta\cos\phi + i\gamma_1\gamma_4\sin\theta\sin\phi,$$

$$F^2 = i\gamma_2\gamma_4\cos\theta + i\gamma_4\gamma_3\sin\theta\cos\phi + i\gamma_3\gamma_2\sin\theta\sin\phi.$$

The independence, commutation, and unit-square properties of the fermionic operators F^1 and F^2 can be straightforwardly demonstrated. These two fermionic operators uniquely define $|F_{\vec{n}}\rangle$ as a Gaussian state/tensor which in fact is the most general form for four Majorana fermions. The covariance matrix of the state (which is defined as $\Gamma_{ij} = \langle\frac{i}{2}[\gamma_i, \gamma_j]\rangle$) in the $(\gamma_1, \gamma_2, \gamma_3, \gamma_4)$ basis is

$$\Gamma = \frac{1}{2}\begin{bmatrix} 0 & \sin\theta\cos\phi & \cos\theta & \sin\theta\sin\phi \\ -\sin\theta\cos\phi & 0 & -\sin\theta\sin\phi & \cos\theta \\ -\cos\theta & \sin\theta\sin\phi & 0 & -\sin\theta\cos\phi \\ -\sin\theta\sin\phi & -\cos\theta & \sin\theta\cos\phi & 0 \end{bmatrix}.$$

In summary, each qubit measurement in the $\vec{n}$ direction results in a Gaussian tensor supported on virtual legs. In the setup where all but a top boundary of qubits are measured, all degrees of freedom except the top boundary of qubits are contracted (Fig. 10). We show in the SM [32] that the Jordan-Wigner transformation of this boundary qubit state precisely yields the Gaussian tensor network state in which the boundary qubit projections and top row of Majorana contractions are removed (Fig. 10, right). Consequently, performing measurements in the bulk of the toric code and employing a Jordan-Wigner transformation at the boundary results in a remaining state described by a Gaussian tensor network.

In the measured toric code, each quantum trajectory can be represented by $\vec{n}_i$, where $\vec{n}_i$ indicates both the type and the outcome of the measurement when measuring the qubit at site i. In this notation, the type of measurement is encoded in the axis of $\vec{n}$, denoted as $e_{\vec{n}}$, while the measurement result is encoded in the direction of $\vec{n}$ along the axis. The probability of each trajectory arises from two sources. Firstly, there is the classical probability set by the protocol, denoted as $w(e_{\vec{n}})$, representing the probability of selecting measurement axis $e_{\vec{n}}$. If the measurements bases are chosen independently from site to site, the probability of a given set of measurement bases is $w(\{e_{\vec{n}_i}\}) = \prod_i w(e_{\vec{n}_i})$. Secondly, the Born rule for
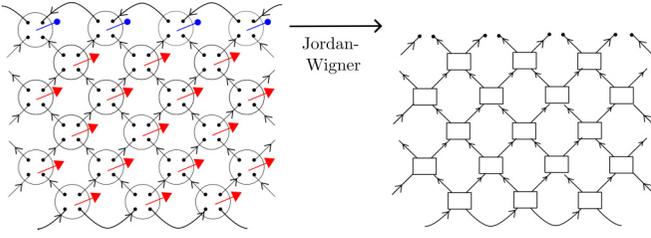
FIG. 10. Bulk measurements of general on-site operators on the toric code ground state can be mapped to a Gaussian circuit on a chain of the virtual Majorana degrees of freedom. The qubit state supported on the top boundary on the left-hand side maps under Jordan-Wigner transformation to the Gaussian state supported on the top boundary on the right-hand side (see Sec. III within the SM [32] for derivation).

the measurement outcome determines the probability $P(\vec{n})$ of the sign associated with $\vec{n}$ based on the measurement. The Born probability $P(\{\vec{n}_i\})$ of each trajectory $\{\vec{n}_i\}$ is the norm of the wave function represented by the tensor network. The combined probability for a particular quantum trajectory is thus $w(\{e_{\vec{n}_i}\})P(\{\vec{n}_i\})$.

This notation can be used to represent the (p, q) measurement protocol for Z, Y, or X measurements discussed in previous sections. Due to axis based definition of w and the fact that $e_{\vec{n}} = e_{-\vec{n}}$, the probability distribution trivially satisfies $w(e_{\vec{n}}) = w(e_{-\vec{n}})$. Therefore, the weights associated with these measurements are $w(e_Z) = w(e_{-Z}) = (1-q)(1-p)$, $w(e_Y) = w(e_{-Y}) = p$, $w(e_X) = w(e_{-X}) = q(1-p)$. Based on the stabilizer formalism, the Born probability for each plus and minus sign is equal to $P(\vec{\sigma}) = \frac{1}{2}$. Consequently, $\sum_{\vec{\sigma}} w(e_{\vec{\sigma}})P(\vec{\sigma}) = 1$. Also note that the classical probability satisfies: $\sum_{e_{\vec{\sigma}}} w(e_{\vec{\sigma}}) = w(e_X) + w(e_Y) + w(e_Z) = 1$.

C. Measured toric code as a Gaussian hybrid circuit

The Gaussian tensors in the virtual space can be understood as Gaussian operations that perform nonunitary transformations between the lower and upper legs of the virtual space, as illustrated in Fig. 9(b). Building upon this observation, we establish a correspondence between a specific class of nonunitary Gaussian circuits in 1+1d and the random Gaussian tensor networks in 2d discussed in the previous section.

These Gaussian circuits are characterized by a set of operators $\{K_{\vec{n}}\}$ and a probability distribution $\tilde{w}(\vec{n})$ associated with the operations. The operators $K_{\vec{n}}$ act on the neighboring Majorana modes γ_i and γ_{i+1} within the virtual space, resulting in nonunitary Gaussian circuits [22,23]. More explicitly, these operators can be expressed as

$$K_{\vec{n}} = \left(1 - n_x^2\right)^{1/4} e^{-i\alpha(\vec{n})\gamma_i\gamma_{i+1}}, \quad (16)$$

where $\alpha(\vec{n})$ is defined by

$$e^{-2\mathrm{Re}[\alpha(\vec{n})]} = \left(\frac{1+n_x}{1-n_x}\right)^{1/2}; e^{i2\mathrm{Im}[\alpha(\vec{n})]} = \frac{in_y + n_z}{(n_y^2 + n_z^2)^{1/2}}. \quad (17)$$

It is worth noting that when n_x is zero, the operations are unitary. However, when n_x is ± 1, the operations correspond to fermion parity measurements. For general $\vec{n}$ with $n_x \neq 0$, the nonunitary operation $K_{\vec{n}}$ is a weak measurement of the

fermion parity. The spacetime geometry of the monitored Gaussian circuit acting on a Majorana chain is depicted in the right-hand side of Fig. 10, and each operation is randomly chosen from the set of operations $K_{\vec{n}}$. The probability of each trajectory is determined by two sources: the classical distribution $\tilde{w}(\vec{n}_i)$ and the Born probability $\langle\psi| K_{\vec{n}_i}^\dagger K_{\vec{n}_i} |\psi\rangle$, where $|\psi\rangle$ is the normalized wave function of the 1d fermion chain before the action of the operator $K_{\vec{n}_i}$, and the updated wave function after the action is given by $\frac{K_{\vec{n}_i}|\psi\rangle}{||K_{\vec{n}_i}|\psi\rangle||}$. Note that the classical probability should satisfy $\tilde{w}((n_x, n_y, n_z)) = \tilde{w}((-n_x, n_y, n_z))$ to not force any bias on the measurement outcomes.

The first step in establishing the correspondence is to relate the operator representation of the tensor $|F_{\vec{n}}\rangle$ in the tensor network to the set of operators in the Gaussian circuit. By performing explicit contractions of the tensor network, it can be shown that the operator representation of the tensor $|F_{\vec{n}}\rangle$ is $\frac{K_{\vec{n}}}{\sqrt{2}}$. This implies that the final state of the hybrid circuit and the tensor network, given the same set of directions, are equal up to a normalization factor. However, this normalization factor is only relevant for the probability of the trajectory. This mapping establishes a direct correspondence between the measurement directions and outcomes (labeled by $\vec{n}$) and a family of operators in the circuit representation parameterized by $\vec{n}$ (Fig. 10).

The second step is to establish a connection between $\tilde{w}(\vec{n})$ and $w(e_{\vec{n}})$ such that identical space-time configurations in both setups have the same probability. The probability of a specific trajectory in the tensor network can be expressed as $P_{\{\vec{n}_i\}} = \prod_i w(e_{\vec{n}_i})|| \prod_i \frac{K_{\vec{n}_i}}{\sqrt{2}} |\psi_0\rangle ||^2$, $|\psi_0\rangle$ being the initial state/lower boundary of the toric code. By recursively defining $|\psi_t\rangle = \frac{K_{\vec{n}_t}|\psi_{t-1}\rangle}{||K_{\vec{n}_t}|\psi_{t-1}\rangle||}$ the probability can be written as $P_{\{\vec{n}_i\}} = \prod_t \frac{w(e_{\vec{n}_i})}{2}||K_{\vec{n}_t}|\psi_{t-1}\rangle ||^2$, which establishes the correspondence with the trajectory probability in the circuit representation.

The $w(e_{\vec{n}})$ ensemble of measurements on toric code is thus the same as the $\tilde{w}(\vec{n}) = \frac{w(e_{\vec{n}})}{2}$ ensemble of nonunitary circuits on Majorana fermions, where the Gaussian operations $K_{\vec{n}}$ are sampled with protocol probability $\tilde{w}(\vec{n})$ [with the restriction $\tilde{w}(\vec{n}) = \tilde{w}(-\vec{n})$]. This establishes the mapping between the measurement protocol on toric code and a specific class of nonunitary Gaussian circuits on the virtual space. However, it is important to note that the integration domains for $\tilde{w}(\vec{n})$ and $w(e_{\vec{n}})$ are different. While $w(e_{\vec{n}})$ is defined over a hemisphere due to its axis-based definition, $\tilde{w}(\vec{n})$ is defined over the entire sphere.

D. Phase diagram of boundary MIE after general on-site measurement

Following the circuit mapping that connects different measurement protocols on toric code with Gaussian fermionic circuits, we can readily use results of the entanglement phase diagram of nonunitary Gaussian circuits to infer the phase diagram of the MIE in the boundary state after measuring the bulk of the toric code state on a cylinder, along any general directions. The corresponding circuit problem has been extensively studied both numerically and analytically recently, e.g., see [22–24]. Corresponding to any Gaussian circuit ensemble

that satisfies the condition $\tilde{w}(\vec{n}) = \tilde{w}(-\vec{n})$, we can find the bulk measurement protocol on the toric code that realizes that Gaussian circuit, via Eq. (17).

These studies have found the entanglement phase diagram to consist of regions of area law and critical logarithmic scaling separated by phase transitions, and we infer that the boundary MIE phase diagram also behaves similarly. This demonstrates that the MIE phase diagram we obtained by mapping the result of specific measurement protocol (along X, Y, or Z directions) to the CPLC model, is qualitatively robust to modifications of the measurement protocol to general on-site measurements. However, the specific phase boundaries and the nature of the phase transition between the area law and critical phases vary between different ensembles, as discussed in [23].

VIII. DISCUSSION

We explored the use of the measurement-based quantum computing (MBQC) setup for generating and manipulating quantum phases of matter. Specifically, we focused on the toric code, a topologically ordered state, and mapped the effects of random Pauli measurements to a classical loop model, allowing for an analytical understanding for measurement-induced entanglement. Additionally, we mapped general on-site measurements to Gaussian tensor networks and hybrid circuits.

We found that the entanglement pattern imprinted on the unmeasured qubits following measurement of the bulk of the toric code ground state undergoes a phase transition that reflects the transition in the corresponding classical loop model. When a boundary chain of qubits is left unmeasured, the boundary state can have either area law or logarithmic scaling of entanglement entropy, depending on the relative X, Y, Z Pauli measurement frequencies. Additionally, we found that these states can also be distinguished by a spin-glass order parameter. This allowed us to devise an adaptive protocol conditioned on the measurement results, which can steer the boundary state into a ferromagnetically ordered state, and this can be efficiently probed in experiments.

Because of the relative simplicity of bulk single-site measurements and the fact that toric code states have already been realized in quantum hardware [35,36], the setup described in this paper are experimentally relevant. Our MBQC-based setup provides a way to simulate $d + 1$-spacetime dimensional hybrid circuits by one layer of local measurements on

a $d + 1$ dimensional entangled resource states. In quantum devices with limited coherence times, this setup may provide a promising practical route towards simulating such hybrid circuits.

Our paper illustrates how parton constructions can be leveraged in MBQC schemes, and it is worth exploring generalizations especially in higher-dimensional resource states. For example, fracton orders admit Majorana parton descriptions [37,38], and one can consider the effect of measurements on such states. Another noteworthy example is the Levin-Wen 3D plaquette model [39], which serves as a natural generalization of the projection of a free-parton state prepared on the edges. One can analyze the effect of measurements by a very similar mapping to a loop model in three dimensions. Furthermore, considering higher dimensional unmeasured manifolds might lead to more complex entanglement structures.

It is also interesting to investigate the relation between measurement-induced entanglement (MIE) in random bases to other aspects of wavefunction complexity. For example, MIE after measurements in a fixed basis can diagnose the sign structure in that particular basis [30], and randomizing the measurement bases may partially probe the robustness of the sign structure to local unitary transformations ("intrinsic sign structure"). There may also be connections between the universality of the resource state in MBQC and the entanglement pattern induced by measurement. For example, a similar bulk measurement protocol on cluster states, which are universal MBQC resources, leads to a phase transition between area- and volume-law states [18]. This can be contrasted with the toric code case (which is not a resource for universal MBQC) in this paper, where any subregion of the boundary state has at most logarithmic scaling of entanglement entropy.

[1] D. Aharonov, Quantum to classical phase transition in noisy quantum computers, Phys. Rev. A **62**, 062311 (2000).

[2] Y. Li, X. Chen, and M. P. A. Fisher, Quantum Zeno effect and the many-body entanglement transition, Phys. Rev. B **98**, 205136 (2018).

[3] B. Skinner, J. Ruhman, and A. Nahum, Measurement-induced phase transitions in the dynamics of entanglement, Phys. Rev. X **9**, 031009 (2019).

[4] Y. Li, X. Chen, and M. P. A. Fisher, Measurement-driven entanglement transition in hybrid quantum circuits, Phys. Rev. B **100**, 134306 (2019).

[5] M. J. Gullans and D. A. Huse, Dynamical purification phase transition induced by quantum measurements, Phys. Rev. X **10**, 041020 (2020).

[6] A. Zabalo, M. J. Gullans, J. H. Wilson, S. Gopalakrishnan, D. A. Huse, and J. H. Pixley, Critical properties of the measurement-induced transition in random quantum circuits, Phys. Rev. B **101**, 060301(R) (2020).

[7] Y. Li, X. Chen, A. W. W. Ludwig, and M. P. A. Fisher, Conformal invariance and quantum nonlocality in critical hybrid circuits, Phys. Rev. B **104**, 104305 (2021).

[8] C.-M. Jian, Y.-Z. You, R. Vasseur, and A. W. W. Ludwig, Measurement-induced criticality in random quantum circuits, Phys. Rev. B **101**, 104302 (2020).

[9] Y. Bao, S. Choi, and E. Altman, Theory of the phase transition in random unitary circuits with measurements, Phys. Rev. B **101**, 104301 (2020).

[10] M. P. Fisher, V. Khemani, A. Nahum, and S. Vijay, Random quantum circuits, Annu. Rev. Condens. Matter Phys. **14**, 335 (2023).

[11] A. C. Potter and R. Vasseur, Entanglement dynamics in hybrid quantum circuits, in *Entanglement in Spin Chains*, edited by A. C. Potter and R. Vasseur (Springer International Publishing, Cham, 2022), pp. 211–249.

[12] S. Sang and T. H. Hsieh, Measurement-protected quantum phases, Phys. Rev. Res. **3**, 023200 (2021).

[13] A. Lavasani, Y. Alavirad, and M. Barkeshli, Measurement-induced topological entanglement transitions in symmetric random quantum circuits, Nat. Phys. **17**, 342 (2021).

[14] A. Lavasani, Z.-X. Luo, and S. Vijay, Monitored quantum dynamics and the Kitaev spin liquid, arXiv:2207.02877v1.

[15] A. Sriram, T. Rakovszky, V. Khemani, and M. Ippoliti, Topology, criticality, and dynamically generated qubits in a stochastic measurement-only Kitaev model, Phys. Rev. B **108**, 094304 (2023).

[16] R. Raussendorf, D. E. Browne, and H. J. Briegel, Measurement-based quantum computation with cluster states, Phys. Rev. A **68**, 022312 (2003).

[17] A. Y. Kitaev, Fault-tolerant quantum computation by anyons, Ann. Phys. **303**, 2 (2003).

[18] H. Liu, T. Zhou, and X. Chen, Measurement-induced entanglement transition in a two-dimensional shallow circuit, Phys. Rev. B **106**, 144311 (2022).

[19] Y. Guo, J.-H. Zhang, Z. Bi, and S. Yang, Triggering boundary phase transitions through bulk measurements in 2d cluster states, Phys. Rev. Res. **5**, 043069 (2023).

[20] J. Behrends, F. Venn, and B. Béri, Surface codes, quantum circuits, and entanglement phases, Phys. Rev. Res. **6**, 013137 (2024).

[21] T.-C. Lu, Z. Zhang, S. Vijay, and T. H. Hsieh, Mixed-state long-range order and criticality from measurement and feedback, PRX Quantum **4**, 030318 (2023).

[22] C.-M. Jian, B. Bauer, A. Keselman, and A. W. W. Ludwig, Criticality and entanglement in non-unitary quantum circuits and tensor networks of non-interacting fermions, arXiv:2012.04666v2.

[23] C.-M. Jian, H. Shapourian, B. Bauer, and A. W. W. Ludwig, Measurement-induced entanglement transitions in quantum circuits of non-interacting fermions: Born-rule versus forced measurements, arXiv:2302.09094v1.

[24] J. Merritt and L. Fidkowski, Entanglement transitions with free fermions, Phys. Rev. B **107**, 064303 (2023).

[25] X.-G. Wen, Quantum orders in an exact soluble model Phys. Rev. Lett. **90**, 016803 (2003).

[26] A. Kitaev, Anyons in an exactly solved model and beyond, Ann. Phys. **321**, 2 (2006).

[27] D. Gottesman, The Heisenberg representation of quantum computers, in *Proceedings of the XXII International Colloquium on Group Theoretical Methods in Physics*, 1999, edited by S. P. Corney, R. Delbourgo, and P. D. Jarvis (Interantional Press, Cambridge, MA, 1998), pp. 32–43.

[28] S. Aaronson and D. Gottesman, Improved simulation of stabilizer circuits, Phys. Rev. A **70**, 052328 (2004).

[29] A. Nahum, P. Serna, A. M. Somoza, and M. Ortuño, Loop models with crossings, Phys. Rev. B **87**, 184204 (2013).

[30] C.-J. Lin, W. Ye, Y. Zou, S. Sang, and T. H. Hsieh, Probing sign structure using measurement-induced entanglement, Quantum **7**, 910 (2023).

[31] A. Nahum, J. Ruhman, S. Vijay, and J. Haah, Quantum entanglement growth under random unitary dynamics, Phys. Rev. X **7**, 031016 (2017).

[32] See Supplemental Material at http://link.aps.org/supplemental/10.1103/PhysRevB.109.125148 We have established a relation between Jordan-Wigner and Parton construction and studied the effect of projection to the physical Hilbert space, Ref. [40]

[33] S. Sang, Y. Li, T. Zhou, X. Chen, T. H. Hsieh, and M. P. A. Fisher, Entanglement negativity at measurement-induced criticality, PRX Quantum **2**, 030313 (2021).

[34] S. Bravyi and R. Raussendorf, Measurement-based quantum computation with the toric code states, Phys. Rev. A **76**, 022304 (2007).

[35] G. Semeghini, H. Levine, A. Keesling, S. Ebadi, T. T. Wang, D. Bluvstein, R. Verresen, H. Pichler, M. Kalinowski, R. Samajdar *et al.*, Probing topological spin liquids on a programmable quantum simulator, Science **374**, 1242 (2021).

[36] K. J. Satzinger, Y.-J. Liu, A. Smith, C. Knapp, M. Newman, C. Jones, Z. Chen, C. Quintana, X. Mi, A. Dunsworth *et al.*, Realizing topologically ordered states on a quantum processor, Science **374**, 1237 (2021).

[37] T. H. Hsieh and G. B. Halász, Fractons from partons, Phys. Rev. B **96**, 165105 (2017).

[38] G. B. Halász, T. H. Hsieh, and L. Balents, Fracton topological phases from strongly coupled spin chains, Phys. Rev. Lett. **119**, 257202 (2017).

[39] M. Levin and X.-G. Wen, Fermions, strings, and gauge fields in lattice spin models, Phys. Rev. B **67**, 245316 (2003).

[40] S. Bravyi, Lagrangian representation for fermionic linear optics, Quantum Inf. Comp. **5**, 216 (2004).